Visualization of Synaptic Markers in the Optic Neuropils of *Drosophila* Using a New Constrained Deconvolution Method

PETER ROBIN HIESINGER,[1]* MICHAEL SCHOLZ,[2]* IAN A. MEINERTZHAGEN,[3]
KARL-FRIEDRICH FISCHBACH,[1] AND KLAUS OBERMAYER[2]
[1]Institute for Biology III, University of Freiburg, D-79104 Freiburg, Germany
[2]Department of Computer Science, Technical University Berlin, D-10587 Berlin, Germany
[3]Neuroscience Institute, Life Sciences Centre, Dalhousie University, Halifax, Nova Scotia, B3H 4J1 Canada

ABSTRACT

The fruitfly *Drosophila melanogaster* offers compelling genetic advantages for the analysis of its nervous system, but cell size precludes immunocytochemical analysis of wild-type structure and mutant phenotypes beyond the level of neuronal arborizations. For many antibodies, especially when immunoelectron microscopy is not feasible, it would therefore be desirable to extend the resolution limit of confocal microscopy as far as possible. Because high-resolution confocal microscopy suffers from considerable blurring, so-called deconvolution algorithms are needed to remove, at least partially, the blur introduced by the microscope and by the specimen itself. Here, we present the establishment and application of a new deconvolution method to visualize synaptic markers in *Drosophila* optic neuropils at the resolution limit of light. We ascertained all necessary parameters experimentally and verified them by deconvolving injected fluorescent microspheres in immunostained optic lobe tissue. The resulting deconvolution method was used to analyze colocalization between the synaptic vesicle marker neuronal synaptobrevin and synaptic and putative synaptic markers in photoreceptor terminals. We report differential localization of these near the resolution limit of light, which could not be distinguished without deconvolution. J. Comp. Neurol. 429: 277–288, 2001.   © 2001 Wiley-Liss, Inc.

Indexing terms: visual system; photoreceptor; synaptobrevin; syntaxin; cysteine string protein; IrreC-rst; confocal microscopy

A single *Drosophila* optic lobe, which is less than 200 μm in diameter, nevertheless contains ∼60,000 cells (Hofbauer and Campos-Ortega, 1990), the neurons of which have cell bodies residing in cortices, with arborizations that extend into four neuropils (for review see Meinertzhagen and Hanson, 1993). The neurons and their arborizations are very small, having a density of packing that exceeds by severalfold the highest density found among vertebrate neurons (for review see Strausfeld and Meinertzhagen, 1998). Although the fly's small size, combined with its developmental and behavioral complexity and the availability of sophisticated genetic tools, provide many experimental advantages, the analysis of neuronal fine structure, combined with the need to examine synaptic connections, is difficult. The small size of cells in the *Drosophila* brain inevitably prescribes dauntingly laborious electron microscopic (EM) studies. Indeed, the high cost and labor-intensiveness of quantitative EM usually exceed the analytical power that this approach can bring to the analysis of neuronal phenotypes. Light microscopy would thus be highly desirable, especially when mutant phenotypes are to be compared in immunostained prepa-

rations or transgenic flies are to be used that express green fluorescent protein (GFP; see, e.g., Timmons et al., 1997). Conventional confocal microscopy currently offers the highest resolution among commercially available light microscopes. The optical resolution is limited by the excitation wavelength, which is two times longer in two-photon confocal microscopy (for review see Denk et al., 1995). Unfortunately, the blurring of high-resolution confocal microscopy scans is of sufficient severity when one tries to image subcellular organelles, such as synaptic contacts, that the interpretation becomes a problem. Further computational effort is therefore needed to improve image quality for such applications, through the use of so-called deconvolution algorithms (Richardson, 1972; Holmes, 1988). Series of optical sections obtained with confocal laser scanning can be used to reconstruct and visualize structures in their three-dimensional entirety. The analysis of small structures close to the resolution limit of light microscopy requires knowledge of imperfections caused by the objective lens and by light scattering along the path of the laser beam (including scatter within the specimen itself). These effects are summarized by the point spread function (PSF), which depends strongly both on the optical setup and on the preparation under consideration (Gibson and Lanni, 1992; Scholz et al., 1998). PSFs can be measured for so-called nonblind deconvolution. Alternatively, if (as here) it is not possible to calculate or measure the PSF reliably, PSFs can be estimated and adjusted to the data during the actual process of deconvolution. In that case one has to estimate the PSF based solely on information given by the degraded image. This method is known as *blind deconvolution* (Lane and Bates, 1987).

To visualize synaptic markers in optic neuropils, we applied a modified blind deconvolution algorithm. The first optic neuropil, the lamina, is one of the anatomically best characterized of *Drosophila* neuropils. It provides an orderly array of modules called cartridges, each of which exclusively contains a single representative of all columnar cell types, each of which in turn has an unambiguous morphological signature (Fischbach and Dittrich, 1989; Meinertzhagen and O'Neil, 1991). This neuropil poses an appropriate challenge to the method, because cross sections of photoreceptor terminals R1–R6 in the lamina have a diameter of about 1 μm and because these terminals each form so-called tetrad synapses that respect a minimum spacing between nearest-neighbor sites of as little as 500 nm (Meinertzhagen and Hu, 1996). This distance thus lies close to the resolution limit for the excitation wavelengths most frequently used in confocal microscopy. High-resolution colocalization analysis of markers for synaptic molecules provides the possibility of relating morphological data to functional data. The more complex structure of the second neuropil, or medulla, although structurally less well characterized, tests the application in its ability to resolve successive strata of extremely fine neurites (Fischbach and Dittrich, 1989), the caliber of which is typical of many other brain regions in *Drosophila*.

In this study, we visualized synaptic markers in the terminals of visual system neurons at the resolution limit of light, by establishing and applying a new deconvolution method. Among other markers, we chose the synaptic vesicle protein neuronal synaptobrevin (n-Syb) and the presynaptic membrane protein syntaxin (Syx). N-Syb and Syx form together with SNAP-25 the so-called core com-

plex, which is sufficient for membrane fusion (Weber et al., 1998) and necessary for neurotransmitter release (for review see Pennetta et al., 1999), and these two proteins are expressed in the developing as well as the adult optic lobe neuropils (Hiesinger et al., 1999; unpublished observations). In contrast to n-Syb, Syx is necessary for cellularization in the embryo (Burgess et al., 1997) and viability of photoreceptors (Schulze and Bellen, 1996; Stowers and Schwarz, 1999). To evaluate the accuracy of deconvolution, the algorithm was first tested by deconvolving fluorescent microspheres after these were injected into the developing optic lobes in the pupal stage of the life cycle and then verified by comparing deconvolved immunostain images to corresponding ultrastructural data. We observed compartmentalized expression, partial colocalization, and also differential distribution of the synaptic markers used, which suggest both overlapping and distinct functions of these molecules. The new deconvolution method provides a reliable means to find and compare functional units of synaptic vesicle trafficking machinery in adult and developing neuropils. Together with existing knowledge of lamina ultrastructure, photoreceptor terminals in particular are highly eligible as models to categorize and characterize new molecules associated with neurotransmission.

MATERIALS AND METHODS
Fly strains and conditions of culture

We used the Gal4/UAS system (for review see Brand and Dormand, 1995) for the expression of photoreceptor-specific n-syb-GFP fusion protein with the following strains: GMR-Gal4 (Freeman, 1996; obtained from the Bloomington Stock Center) and UAS-n-Syb-GFP (Ito et al., 1998; Estes et al., 2000; obtained from M. Ramaswami). Wild-type Berlin was used as the wild-type stock. Flies were raised at 25°C (at which 100% pupal development corresponds to 103 hours after pupation).

Immunohistochemistry, confocal microscopy, and image processing

Adult brains were prepared and stained as described by Hiesinger et al. (1999). The following dilutions of antibodies were used: anti-n-Syb, 1:100; mab 8C3 (anti-Syntaxin), 1:100; mab 24A5 (anti-IrreC-rst), 1:50; mab 49 (anti-csp), 1:50; and mab 24B10 (anti-Chaoptin), 1:50. A Leica TCS4D and a Zeiss LSM 510 confocal microscope were used for data acquisition. Series of complete optic lobes comprising 64–200 images of 512 × 512 pixel resolution at eight-bit color depth were scanned through a 100×/1.4 planapochromat objective. Subsets of such data were processed on an SGI Octane MXI workstation using the three-dimensional (3D) visualization software Amira (Indeed GmbH, Berlin, Germany). Techniques used were maximum-intensity projection and volume rendering. Figures were assembled and labeled in Adobe Photoshop.

Microinjection of fluorescent microspheres

Adult brains were prepared and stained with anti-n-Syb as described above. Just prior to coverslipping, brains received injections while in Vecta Shield mounting medium (Vector Laboratories, Burlingame, CA). We used red fluorescent microsphere beads (Molecular Probes, Eugene, OR) 500 nm in diameter, at various dilutions in Vecta Shield, microinjected with an Eppendorf Transjector 5246.
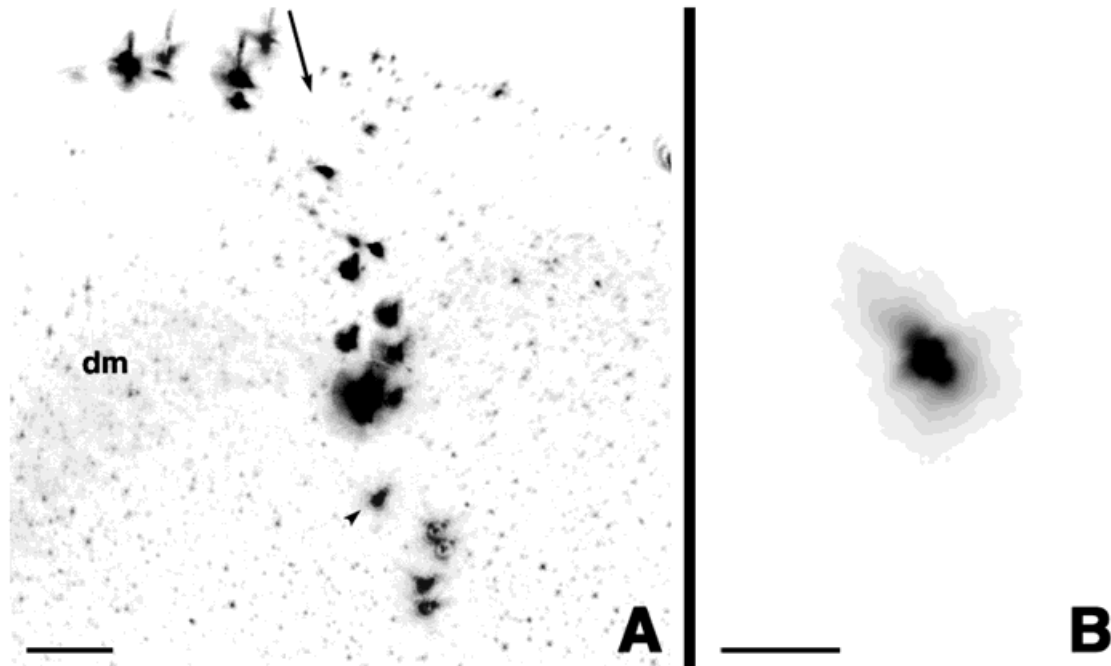
Fig. 1. Fluorescent microspheres injected in an n-Syb-stained optic lobe. **A:** High-resolution scan at the site of microsphere injection. An arrow marks the site and the direction from which the brain was penetrated by the injection. **B:** Enlargement of the microsphere marked with an arrowhead in A, shown in a maximal projection that includes the complete light distribution along the optical axis. Rays of scattered light from the fluorescent bead are irregular, and the spherical shape is significantly disturbed. Deconvolution parameters were tested by deconvolving the images of these beads (cf. Fig. 3). dm, Distal medulla. Scale bars = 10 μm in A, 2 μm in B.

Glass capillaries were produced using a vertical pipette puller and with inspection under a stereo microscope were broken to a sharp tip.

Implementation and application of the deconvolution algorithm

We have developed a blind deconvolution algorithm, based on a maximum-likelihood approach (for review see Holmes et al., 1995) under the assumption of poisson-distributed noise (as proposed by Holmes, 1992). The solution for the PSF was constrained to be circularly symmetric in the x,y plane, band-limited, and positive, the latter also being applied to the image. We implemented our deconvolution algorithm in a maximum a posteriori approach (Joshi and Miller, 1993) and regularized the solution using Good's roughness penalty in the form of Verveer and Jovin (1998), extending their algorithm to a blind form. Because it is of great advantage to understand exactly the features of such an algorithm, we opted to implement our own algorithm, which differs slightly from one commercially available product (Holmes, Autoquant).

The algorithm was programmed in C++ and compiled for two Silicon Graphics Octane dual-processor workstations (R10K, 195 MHz; 896 MB and 1,024 MB RAM). Data sets for deconvolution were separated into single channels and cropped to a final size of $256 \times 256 \times 64$ pixel (4 MB). A run of 80 iterations took approximately 4 hours and needed a constant 687 MB of memory on an SGI Octane as described above. Image data and PSF data were viewed and processed with 3D visualization software (Amira; Indeed GmbH).

RESULTS

Parameter sets can be ascertained experimentally that lead to robust blind deconvolution on noisy antibody stainings at the resolution limit of light

The shape of the PSF depends strongly on the characteristics of the particular brain tissue and staining, as reported in a parallel study (Scholz et al., 1998; Scholz, Bucher, Hiesinger, Pflüger, and Obermayer, unpublished observations). We therefore selected a blind deconvolution method using parameters that were subsequently evaluated according to their ability to deconvolve correctly the shape of fluorescent beads of known size and spherical shape, which had previously been injected into immunostained optic lobe tissue. Our deconvolution method performs conservative corrections only to the common and therefore safe parts of the PSF shape pool while adapting to the image data at the same time (Scholz et al., 1998, 1999). To test our method and find parameters that introduced no artifacts, we established the following procedure. First, we injected the fluorescent microspheres into an optic lobe that was already immunostained using an antibody against neuronal synaptobrevin, a synaptic marker for which we sought the distribution at high resolution (Fig. 1A). As in other stained *Drosophila* and locust brain
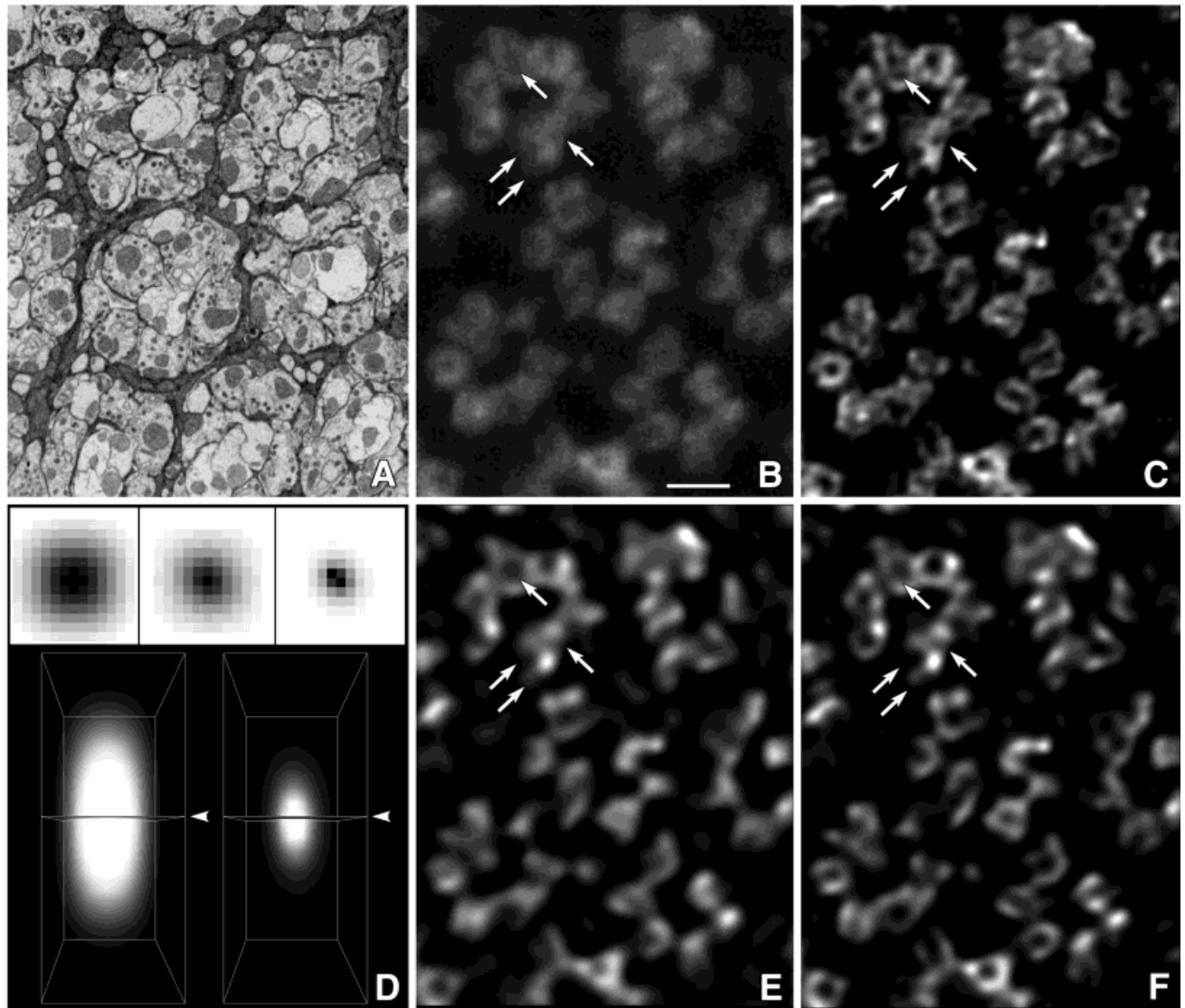
Fig. 2. Deconvolved images of lamina cross sections with photoreceptor-specific n-Syb-GFP expression. **A:** Ultrastructure of a lamina cross section used as a reference to compare to deconvolution images. Within the cartridges a ring of six gray photoreceptor terminals encircles two or three lighter axon profiles of lamina monopolar cells. **B:** Original high-resolution scan of a lamina cross section with photoreceptor-specific n-Syb-GFP expression. Cartridges with a characteristic ring of six photoreceptor terminals can be identified, but compartments of fluorescence within the terminals are blurred. **C:** Best deconvolution result of the data set in B. PSFs used are described in D. The data set is significantly deblurred, and the predominant localization of the fusion protein at the periphery of the terminals' plasmalemmata becomes apparent. Furthermore, subcompartments are recognizable that could, for example, derive from invaginations or mitochondria (cf. arrows with B). **D:** PSFs used for the deconvolution in C. The upper row shows x/y sections of the center of the three-dimensional PSFs, as depicted with arrowheads in the 3D volume reconstructions of the PSFs below. Upper row, left: 16 point (1.28 μm in x/y) PSF was used as a starting function and modified together with the data for 80 iterations, resulting in the PSF shown in the middle. This PSF was used as a starting function for deconvolution of the original image data and the whole procedure repeated a third time, resulting in the PSF shown on the right. The 3D volumes below correspond to the first and the final PSF, respectively. **E:** Deconvolution result after 80 iterations with a 24 point (1.92 μm in x/y) PSF. The image is deblurred and smoothed, but small structures less than ∼1 μm (kernel of the PSF) are artificially fused. **F:** Deconvolution result after 80 iterations with the appropriately sized (16 point) but wrongly shaped (subgaussian instead of supergaussian, medium upper image in D) PSF. The result is only slightly better than in E but significantly worse than with the correctly shaped PSF (C). Scale bar = 2 μm for A–C, E, F.

tissues (unpublished results; D. Bucher, personal communication), PSFs exhibit varying, irregular rays and halos (Fig. 1B). Second, deconvolution parameters were tested and optimized using other image data of the same optic lobe structures. Third, these parameters were verified by testing their effect on the deconvolution of the PSFs of the beads.

When evaluating the results of such blind deconvolutions, criteria are necessary to distinguish correctly the intensified structures from artifacts, for which indepen-

dent information about the ultrastructure is essential. We chose the lamina neuropil, because its regular organization contributes many cartridge cross sections to a single confocal image and because, within each, the contributions of each cell type can be identified (Fig. 2A). This knowledge helps to interpret the staining patterns seen in light microscopy near the resolution limit and offers a good prospect to investigate the localization of synaptic vesicle trafficking molecules in subcompartments of the photoreceptor terminals. To image the terminals we used photoreceptor-specific expression of an n-Syb-GFP fusion protein (Ito et al., 1998; Estes et al., 2000) via the Gal4/UAS system. Raw confocal images show the regular organization of terminals in individual cartridges but with little detail (Fig. 2B).

We tested several parameters for blind deconvolution of the three-dimensional data set, including step width (learning parameter), initial PSF size, and number of iterations. Although different numbers of iterations can largely compensate for step width (data not shown), PSF size and shape have the most significant influence on the deconvolved data. From the observed light scattering of injected 500 nm beads, we calculated a PSF size in voxels and tested the effects that this, together with gradually smaller PSFs, had on deconvolved images. Whereas selecting too large a starting PSF tends to fuse distinct structures, too small a PSF can divide structures arbitrarily, thus introducing artifacts. The resolution limit of light, however, dictates the minimum distance between two resolvable structures. For the data set shown in Figure 2, the voxel distance in x,y was 80 nm, and we tested PSFs between 8 voxel (640 nm) and 24 voxel (1.92 μm) maximal light spread. Deconvolution with a PSF that is 50% too large already results in severe loss of data and emergence of artificial structure (Fig. 2E), as does the choice of a PSF that is too small (data not shown). Deconvolution with a PSF of appropriate size, in our case 16 voxel, still leads to a loss of fine-structural information when the shape is not adapted to the light distribution within the image data (Fig. 2F), again based on recognizably distinct structures in the original image data (Fig. 2B). Because blind deconvolution is an algorithm that uses data to refine the PSF, and the PSF to refine the data in an iterative process, the image data can already be severely adulterated when the PSF reaches an appropriate shape. Hence we took only the resulting PSF of the deconvolution with the appropriately sized PSF, from which Figure 2F is derived, and used it as a new starting PSF for the original image data, thus stabilizing the solution. The same procedure was repeated three times consecutively, until comparison of the deconvolved image data to the original image data no longer displayed obvious loss of fine-structural detail. The result is an unblurred, high-resolution cross section (Fig. 2C) within which ≥400 nm subcompartments are still recognizable and that corresponds in its appearance to details recognizable in EM cross sections (Fig. 2A).

Finally, we used the method described with all ascertained parameters to deconvolve the confocal scans of beads shown in Figure 1. The success of the deconvolved data sets, which for the bead in Figure 1B is shown in Figure 3, reflects the chosen approach not to correct for outer rays and halos of light scattering, which differ significantly within the tissue, but instead to correct the kernel and safely assignable parts of the PSF. The parameters thus ascertained to initiate the blind deconvolution, which then iteratively optimizes specific data, were used for all following analyses.
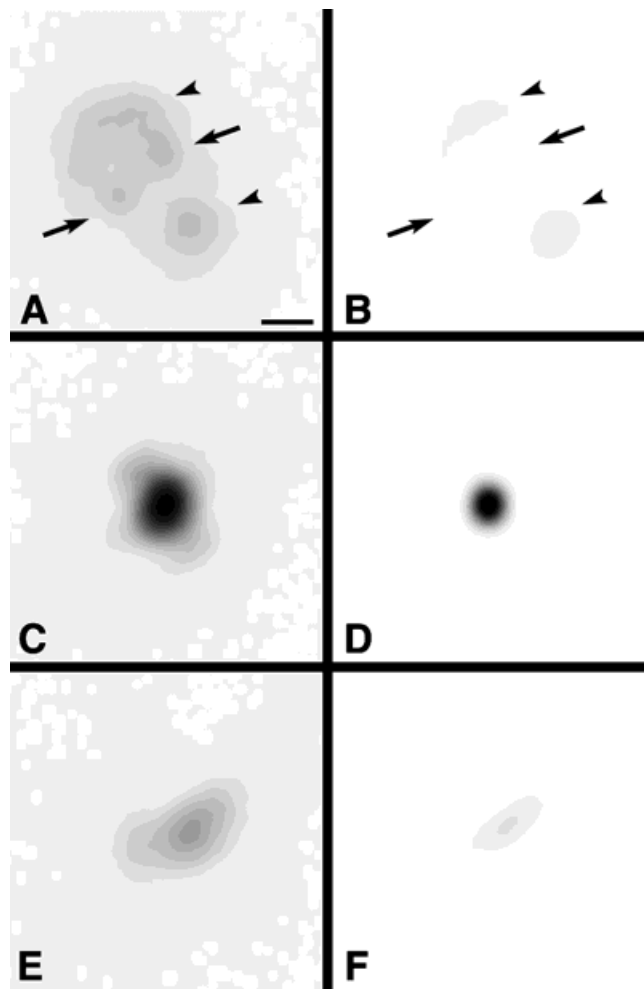

Fig. 3. Deconvolution of the 500 nm microsphere in immunostained optic lobe tissue shown in Figure 1B. **A,B:** Cross section of the light scattering 3 μm above the center of the bead (towards the objective). Irregular rays of scattered light arise from the original image (A). Two of these in the center are completely removed by the deconvolution (cf. arrows in A and B), because they were safely recognized as part of the bead's point spread function. In contrast, outer rays are diminished but not removed (arrowheads), ensuring the avoidance of artifacts. **C,D:** Cross section through the center of the bead. The irregular shape and rays of light scattering in the original image (A) are completely corrected after deconvolution (D). **E,F:** Three micrometers beneath the center of the bead, light scattering is again partly corrected but not completely removed. Scale bar = 1 μm.

Smoothing constraints are required to stabilize the solution of blind deconvolutions in three dimensions

The deconvolution method we use is based on 3D data sets, so light scattering in all three dimensions is evaluated to intensify the actual structure and diminish or eliminate artifactual blur. All the confocal images presented in Figures 2 and 4–6 are single confocal sections. The results of a deconvolution cannot be understood solely
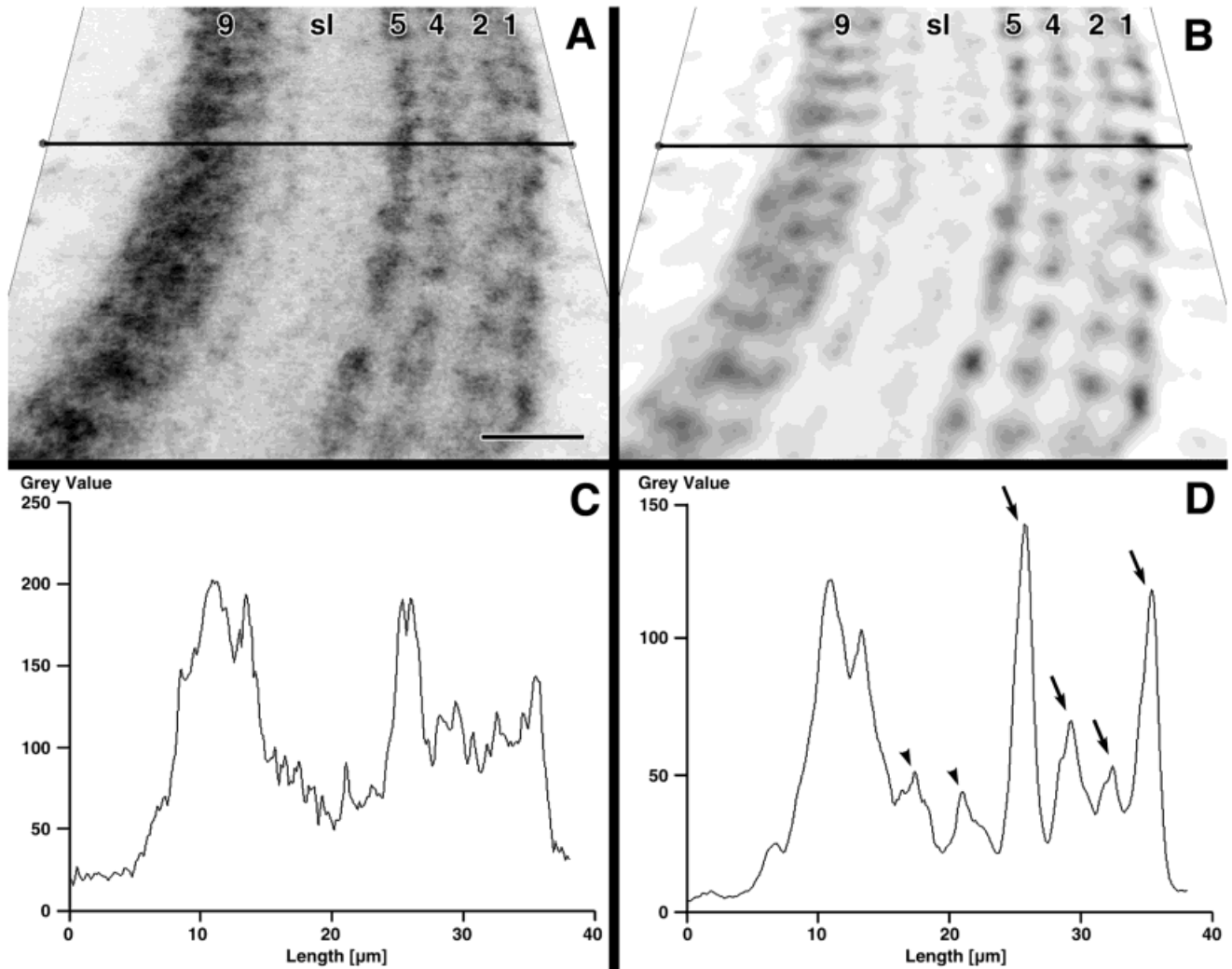
Fig. 4.   Deconvolution of neuropil fine structure with smoothing constraint. **A,B:** Medulla sections from an image stack of a midpupal brain immunostained with anti-IrreC-rst, either before (A) or after (B) deconvolution with Good's roughness as a smoothing constraint. Lines indicate vertical transects through the neuropil, for which image density is plotted in C and D. **C,D:** Plots of density, shown as gray-scale value (0–255), for the transects marked in A and B. The four medulla layers, 1, 2, 4, and 5, that are stained by anti-IrreC-rst are clearly intensified as plausible 3D structures in the data set (arrows in D). Additionally, two layers around layer 7 (the serpentine layer) become apparent that were hitherto unrecognized (arrowheads in D). 1, 2, 4, 5, Medulla layers; sl, serpentine layer. Scale bar = 5 μm in A,B.

by comparing such single sections as original and deconvolved images, however, but only after evaluating complete image stacks. Three-dimensional datasets obviously provide many more opportunities to find plausible light sources and light scattering. Even in 3D datasets, however, irregular blur at or below the resolution limit of light can contain contrasts that are sufficiently strong to be artifactually separated by deconvolution. One solution to this problem is to apply additional constraints. To find a stable solution for the original image that avoids overfitting, we need a general criterion to determine the most plausible estimate. To avoid fitting the noise, a promising criterion is to choose the smoothest solution. This is based on the assumption that neighboring points in the original image are similar and become uncorrelated by noise. In practice, the amount of regularization needed to stabilize the solution by suppression of noise, without sacrificing too much sharpness, has to be ascertained experimentally.

We tested Good's roughness (Good and Gaskins, 1971) as a smoothing constraint. To investigate the application we chose the medulla, because this neuropil has a well-characterized organization into layers and columns (Fischbach and Dittrich, 1989), the small dimensions of which test the validity of the smoothing constraint. We used an antibody against IrreC-rst (Schneider et al., 1995), a previously described marker, to visualize this organization.

The effect of the smoothing constraint can be seen in Figure 4. Medulla layers 1, 2, 4, and 5, which are immunostained by anti-IrreC-rst at the midpupal stage, are clearly separated by the deconvolution. Furthermore, plots of the staining intensity reveal the selectivity of the smoothing and intensification of four peaks corresponding to four strata immunostained by the antibody (Fig. 4A). In addition to these layers, which were previously characterized (Schneider et al., 1995), the constrained deconvolu-
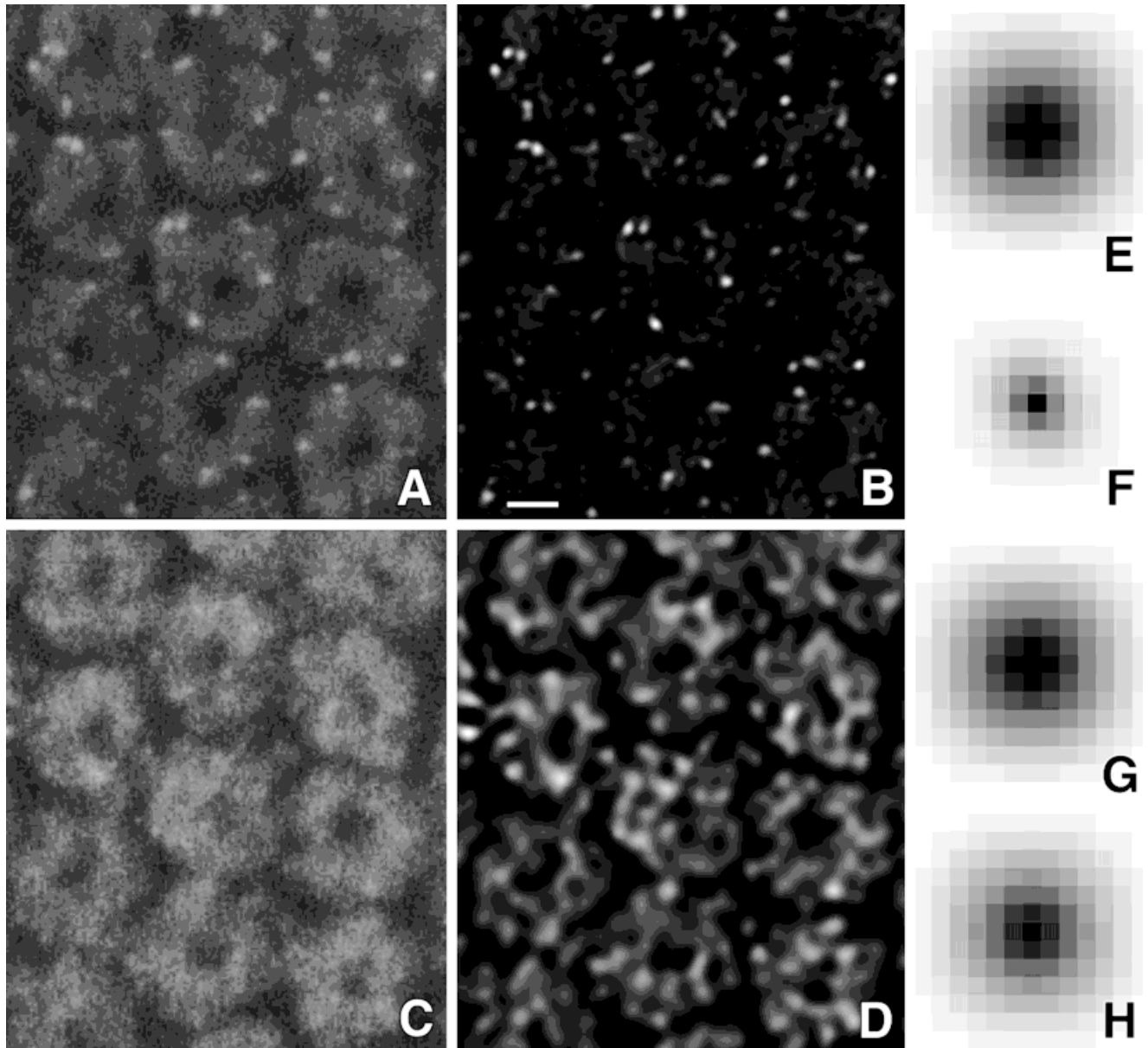
Fig. 5. Deconvolving the single channels of a n-Syb/Syntaxin double stain requires different PSFs. **A:** Original confocal section from the anti-n-Syb image stack. Deconvolution with the PSF depicted in E; results after 80 iterations in the PSF shown in F. **B:** Deconvolution of the original data set with the PSF shown in F as a starting function. **C:** Original confocal section from the anti-Syntaxin image stack. De-convolution with the PSF depicted in G; results after 80 iterations in the PSF shown in H. Because the anti-Syntaxin stain is more diffuse and lacks distinct immunoreactive puncta, of the sort seen with anti-n-Syb, the resulting PSF is much wider. **D:** Deconvolution of the original data set with the PSF shown in H as a starting function. Scale bar = 2 μm in A–D.

tion reveals two layers of IrreC-rst immunoreactivity at a level corresponding to the serpentine layer (layer 7; Fischbach and Dittrich, 1989) as plausible structures within the 3D image stack that are not apparent in single sections of the data set before deconvolution (Fig. 4A). Based on the validity of Good's roughness smoothing constraint in detecting medulla strata 1, 2, 4, and 5, this finding demonstrates that appropriately smoothed 3D high-resolution data are a superior basis to deconvolve plausible structures in noisy antibody stainings of whole-mounted brains.

PSF shape depends on staining properties, as revealed by lamina neuropil doubly immunostained for Synaptobrevin and Syntaxin

The aim in this study of establishing a safe and powerful method of deconvolution is to analyze the colocalization of markers for synaptic and vesicle trafficking proteins, so we next investigated double stainings using the previously tested method. Figure 5 shows a lamina cross section immunostained with antibodies against neuronal

Synaptobrevin (Deitcher et al., 1998) and Syntaxin (Fujita et al., 1982). Although both stainings reveal the same overall organization in cartridges, the staining patterns differ considerably, with the anti-Syntaxin staining appearing more diffuse (Fig. 5C). As described above, we tested possible PSF starting sizes and evaluated each alteration in the PSF after reiteration with the original data. After the first run, the resulting PSFs exhibited significanty different shapes that reflect properties of the different antibody stainings. The PSF for the more diffuse anti-Syntaxin staining is much less steep than that for anti-n-Synaptobrevin, which incorporates a more distinctly punctate pattern of immunostaining (Fig. 5A,B), demonstrating that the light distribution and correctable blur strongly depend on the properties of the particular staining. We used each of the two PSFs to deconvolve the corresponding channel of the double immunostain using the best parameters ascertained (Fig. 5F,H). Again, the deconvolution intensifies details of the 3D data that are not revealed in the raw confocal images. This is especially apparent for the diffuse anti-Syntaxin staining, in which the outlines of compartments become visible that correspond to the outlines of photoreceptor terminals in the cartridges. These results clearly show that our blind deconvolution method optimizes PSFs for specific antibody stainings when initiated with the same parameters and hence indicate that deconvolution of image stacks from preparations immunostained with different antibodies using a fixed PSF may create artifacts.

Neuronal Synaptobrevin, Syntaxin, and Cysteine String Protein exhibit differential colocalization patterns in lamina cartridges

In the final step of this study, we applied the established deconvolution method to analyze the differential localization and colocalization of selected synaptic vesicle trafficking markers in cartridge cross sections. First, the targeted expression of the n-Syb-GFP fusion protein in photoreceptors was compared with that of an antibody that recognizes n-Syb (Fig. 6A,B). Anti-n-Syb staining reveals a distinct speckled pattern of immunostaining, with strongly immunoreactive puncta (Fig. 5). The GFP fusion protein seems to be poorly recognized by the anti-n-Syb antibody used in this study. Colocalization is observed between some of the puncta and the outline of the terminal picked out by the expression of the fluorescent n-Syb-GFP fusion protein. This partial colocalization between anti-n-Syb puncta and such outlines suggests that the GFP fusion protein is targeted to the terminal plasmalemma, because n-Syb interacts with the target membrane protein Syntaxin. The puncta revealed by n-Syb immunostaining are not found within the interior of the terminals, consistent with them being a marker for synaptic release sites.

To test the latter possibility further, we investigated additional combinations of double immunostaining with anti-n-Syb. Figure 6C,D shows double immunostains of n-Syb with Syntaxin, which are already presented as separate stains (Fig. 5). Again, punctate immunostaining of anti-n-Syb is revealed, with only partial colocalization. Weak immunoreactivity is also detectable in the cytoplasm of the photoreceptor terminals, which is seen in the single-channel images (Fig. 5A,B) but which, because of the color overlay between the two channels, is less apparent in the two-

channel images (Fig. 6A,B). Given that the cytoplasm of photoreceptor terminals is filled with synaptic vesicles (Meinertzhagen and O'Neil, 1991), this pattern is consistent with a vesicular localization of n-Syb. In contrast, there is again strong staining of immunoreactive puncta, with only partial colocalization around the circumference of the receptor terminal profile and elsewhere outside terminals. Frequently neighboring puncta are separated by an edge-to-edge distance of approximately 500 nm, sometimes around the circumference of the terminal profile. Such pairs are compatible with tetrad sites in two ways. First, this distance corresponds to the minimum spacing of 500–600 nm between tetrad synapses in a single terminal (Meinertzhagen and Hu, 1996). Second, the position of such pairs is often at the closest apposition between adjacent terminals and thus corresponds to the common localization of tetrad synapses at opposite sites in neighboring terminals (Meinertzhagen and O'Neil, 1991). Sites outside the circumference of the receptor terminal profile are compatible with synaptic sites in other elements, particularly amacrine cell processes, which also have large numbers of synapses (Meinertzhagen and Sorra, 2000).

The anti-Syntaxin staining reveals a widespread distribution of strong immunoreactivity at the circumference of the terminals' profiles. Photoreceptor terminals are less distinctly recognized by anti-Syntaxin than they are revealed by photoreceptor-specific expression of n-Syb-GFP fusion protein, which putatively interacts with Syntaxin. Instead, anti-Syntaxin immunostains sites of contact between the terminals and their neighbors. Anti-Syntaxin does not, however, stain the cytoplasm of terminals, corresponding to its known localization at the plasmalemma (Schulze and Bellen, 1996). The wider distribution of Syntaxin also indicates that its localization is not restricted to synaptic release sites, implicating it in additional functions. The latter is consistent with Syntaxin's postulated

Fig. 6. Colocalization between synaptic vesicle trafficking and photoreceptor markers in double-labeled preparations with anti-n-Syb. Original confocal images from 3D datasets on the left; corresponding deconvolved data on the right. **A,B:** Photoreceptor-specific expression of n-Syb-GFP and immunoreactivity to n-Syb (green n-Syb-GFP channel; same as in Fig. 2). Anti-n-Syb staining (red) reveals immunoreactive puncta that occasionally colocalize with the outlines of photoreceptor terminals marked by the n-Syb-GFP fusion protein (arrows). **C,D:** Double staining of n-Syb and syntaxin (same data as in Fig. 5). The highly blurred syntaxin channel (green), in particular, reveals significantly clearer structures after deconvolution. In the central cartridge, the six photoreceptor terminals (asterisks in D) are clearly recognizable in the 3D data, which was not possible in the raw confocal image. Immunostained anti-n-Syb puncta are lacking in the interior of terminals but occur occasionally at the circumference of the terminal profile, revealing sites of colocalization (arrows) and differential localization (arrowheads). Neighboring anti-n-Syb-stained puncta separated by about 500 nm (encircled) are frequently found that are clearly resolved in D (cf. lack of clear resolution in C). **E,F:** Anti-CSP and anti-n-Syb double staining. The intensity of the anti-CSP staining is much weaker than either the anti-Syntaxin staining or n-Syb-GFP fluorescence and at a level similar to the weak cytoplasmic staining of anti-n-Syb (cf. Fig. 5A and B). The two stainings of the terminal cytoplasm largely colocalize, whereas the anti-n-Syb immunoreactive puncta do not. **G,H:** Anti-Chaoptin and anti-n-Syb double staining. The deconvolved data reveal that anti-Chaoptin stains the terminal plasmalemma. Some n-Syb-immunoreactive puncta colocalize with the plasmalemmal staining (arrows), whereas others in the vicinity of terminals do not (arrowheads; cf. B and D). Scale bar = 2 μm.
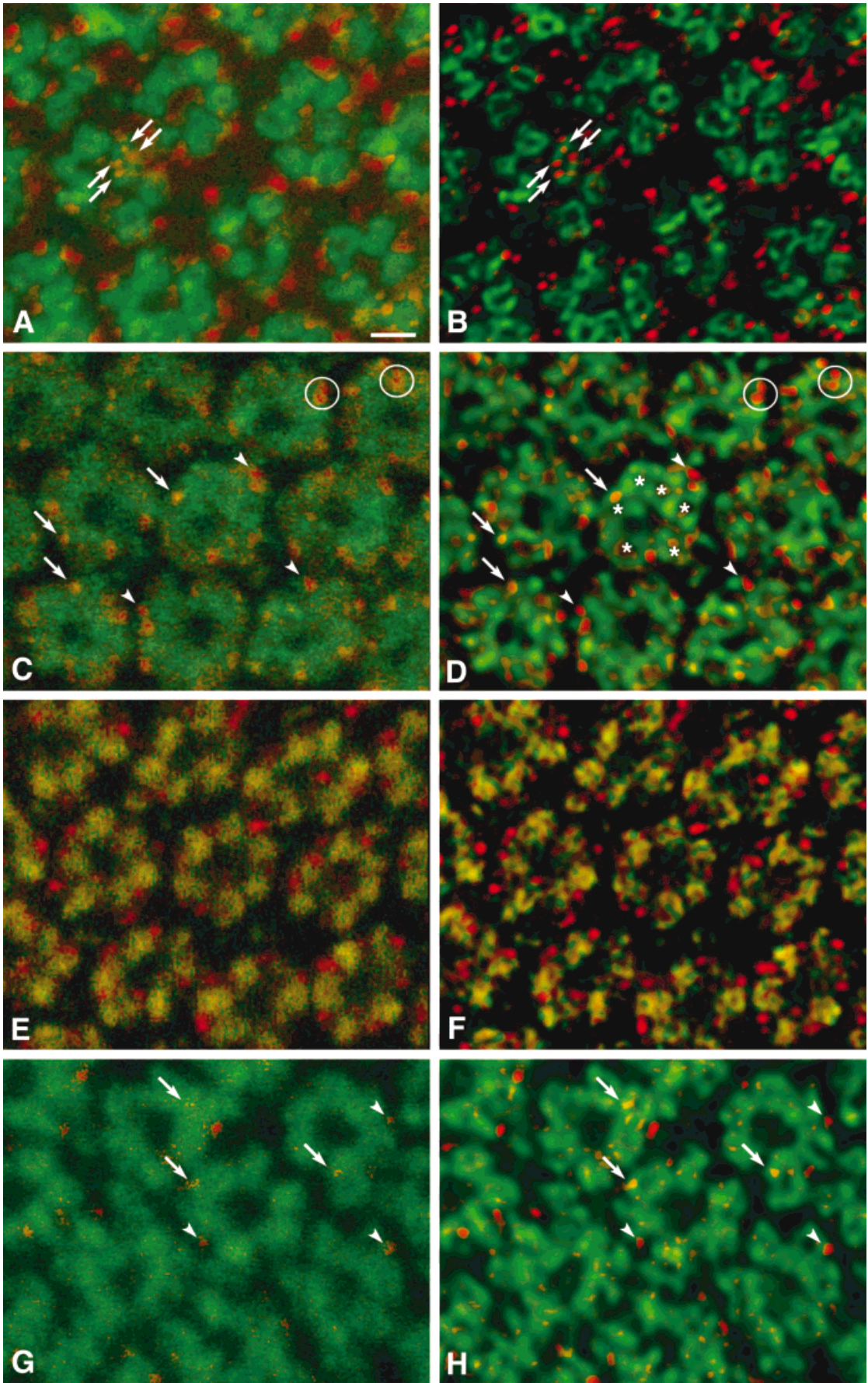
Figure 6

role in membrane formation and stabilization, independent of neurotransmitter release and the requirement of Syntaxin for the viability of photoreceptors (Schulze and Bellen, 1996; Stowers and Schwarz, 1999).

We then compared n-Syb immunostaining with the localization of Cysteine String Protein (CSP), another vesicle-associated molecule of the synaptic vesicle cycle (Zinsmaier et al., 1990). In contrast to larval motor terminals, where n-Syb-GFP and CSP strongly colocalize (Estes et al., 2000), photoreceptor terminals exhibit a differential distribution as revealed in high-resolution deconvolved confocal images. Whereas photoreceptor-specific expression of n-Syb-GFP apparently leads to a specific labeling of terminal plasmalemma, as described above, anti-CSP stains the cytoplasm of the terminal (Fig. 6E,F), corresponding to ultrastructural findings on synaptic boutons of the larval muscle using immunogold labeling (Eberle et al., 1998). The cytoplasmic staining in photoreceptor terminals colocalizes with the weak immunoreactivity to n-Syb, again consistently with the vesicular localization of both molecules. In contrast, as for the double stainings described above, the puncta strongly immunoreactive to n-Syb rarely exhibit such colocalization.

Finally, to analyze the localization of n-Syb-positive immunostaining compared with a plasmalemmal marker, we made double labelings of n-Syb with anti-Chaoptin (Zipursky et al., 1984), an antibody against Chaoptin, a photoreceptor-specific cell adhesion molecule (Van Vactor et al., 1988; Krantz and Zipursky, 1990). Whereas the plasmalemmal localization of Chaoptin is not clearly discernible in raw confocal data (Fig. 6G), it becomes obvious after deconvolution (Fig. 6H). As for the double labelings with anti-Syntaxin and photoreceptor-specific n-Syb-GFP expression, some n-Syb-immunoreactive puncta appear associated with the cartridges but do not colocalize with photoreceptor terminals, whereas others colocalize with the plasmalemmal staining.

In summary, these results show that differential localization of synaptic vesicle markers can be shown by means of confocal microscopy in lamina cartridge cross sections, even within individual photoreceptor terminals, that not only are consistent with known features of these molecules but also through their compartmentalization give indications of additional functions.

DISCUSSION

In this study we have established a new deconvolution method to visualize synaptic markers in the optic neuropils of *Drosophila* at or close to the limit set by the wavelength of visible light. Taking advantage of the size and patterned organization of cartridge profiles in lamina cross sections, we report the differential localization of specific markers for synaptic vesicle trafficking proteins within the anatomically well-characterized terminals of photoreceptors and in the process uncover a pattern of punctate immunoreactivity consistent with, and thus a putative marker for, synaptic release sites or associated organelles.

Deconvolution parameters have to be adapted to the structure and staining of interest

Our results demonstrate that deconvolution is a powerful method to visualize antibody stainings at the resolu-

tion limit of light. For the blind deconvolution algorithm used in this study, however, we show that untutored application of the method can easily create artifacts. For different antibody stainings of the optic neuropils, various parameters have to be adapted differentially, the most important of which are the size and shape of the PSF. The latter varies not only within the same tissue, as shown previously (Scholz et al., 1998), but also for each of the two simultaneous immunostainings, as we show for n-Syb and Syntaxin double-stained tissue. This finding suggests that the stained structures themselves differ in their optical properties (refractive index, scattering coefficient), perhaps in the way in which the primary antibodies bind within the structures. Given that blind deconvolution has been shown to be the safest deconvolution method (Scholz et al., 1998), the implications for its application to immunocytochemical data comparable to those presented in this study are all the more significant. Additional comparisons with fine-structural findings are desirable to evaluate staining patterns and minimize artifactual deconvolution results. Furthermore, ascertaining the correct PSF size and shape has to be carried out separately for each antibody.

Quality of deconvolution is limited by technical constraints of data acquisition with the confocal microscope

Blind deconvolution estimates the PSF as a probability density function from stochastical and noisy data. Insofar as the number of photons reaching the detector of a confocal microscope dramatically decreases with the distance from the focal point, the uncertainty of the PSF estimate also increases as this distance increases. To ensure that there are sufficient data far from the focus in the axial (Z) dimension, one would have to oversample the specimen heavily during data acquisition, leading to severe photobleaching. By constraining our algorithm to estimate only the inner 95% of intensity values, we retain sufficient enhancement laterally while limiting the unavoidable photobleaching. As a consequence of this, however, resolution in the axial dimension is enhanced by only a factor of about 2, which serves as a good compromise in our application.

High-resolution confocal microscopy can be used to visualize the differential localization of synaptic markers in lamina cartridges

Profiles of cross-sectioned photoreceptor terminals vary in diameter between 0.5 μm and 2 μm, so that structural details can be visualized with light microscopy only when it is used at the highest possible resolution. Using markers for different synaptic vesicle trafficking proteins and comparing the distribution of these with EM data for the profiles of photoreceptor terminals, we are able to discriminate protein localization in the cytoplasm from that at the plasmalemma or at contact sites on the terminal.

The expression of the n-Syb-GFP fusion protein has previously been shown to be enriched in neuropils, with fluorescence at larval motor terminals colocalized with CSP and thus localized at synaptic vesicle membrane (Estes et al., 2000). For photoreceptor terminals, however, we find clear targeting of the fusion protein to the plasmalemma of the photoreceptor terminals where it is ex-

pressed, whereas anti-CSP staining is predominantly cytoplasmic. This finding is consistent with the vesicular localization of CSP and the known distribution of synaptic vesicles within photoreceptor terminals (Meinertzhagen and O'Neil, 1991). The localization of the n-Syb-GFP fusion protein in photoreceptor terminals is consistent with its targeting to the plasmalemma, where Syntaxin is also localized. A putative role for Syntaxin in membrane formation or stabilization (Schulze and Bellen, 1996) at photoreceptor terminals could explain the differences between the differential localization of n-Syb-GFP and CSP seen here and the colocalization reported by Estes et al. (2000), supporting what is possibly a photoreceptor-specific distribution of Syntaxin.

The exceptionally clear labeling with n-Syb-GFP of the six photoreceptor terminals in typical nonequatorial cartridges is readily understood from its photoreceptor-specific expression. The n-Syb-GFP pattern clearly supports the pattern of anti-Syntaxin, which also reveals the structure and locations of photoreceptor terminals in cartridges. Additionally, syntaxin is probably also expressed in other cells as well as in photoreceptors. Nevertheless, deconvolution clearly shows the localization of Syntaxin immunoreactivity at the circumference of photoreceptor terminals rather than in their interior. Deconvolution cannot, however, arbitrate on which side of the membrane the protein is localized. It is therefore possible, even in an immunostained preparation that clearly shows the outline of a photoreceptor terminal profile, that the protein is actually expressed in the neurites of postsynaptic lamina cells that encircle the terminal. In contrast, cytoplasmic staining strongly suggests the expression of a protein in the corresponding cell. The finding that CSP is localized mainly in the cytoplasm of photoreceptor terminals is consistent with its known presynaptic role in neurotransmitter release (Zinsmaier et al., 1994).

An antibody against neuronal synaptobrevin is a putative marker for synaptic release sites

Although n-Syb is known to be a vesicle-associated protein, several lines of evidence suggest that an antibody against an oligopeptide unique for n-Syb (Deitcher et al., 1998) could be a marker for synaptic release sites in photoreceptor terminals and/or lamina neurons, or some other punctate organelle with a corresponding distribution. First, the n-Syb-immunoreactive puncta either colocalize with the plasmalemma of photoreceptor terminals or are localized close to them but are not found within the interior of the terminals. Their distribution is thus not consistent, for example, with immunostaining of the terminal's only other punctate synaptic organelles, the capitate projections, which frequently invaginate deeply into the interior of the terminal (Stark and Carlson, 1984). They are often found at sites where neighboring terminals abut, the most frequent location of the photoreceptor's tetrad synapses (Meinertzhagen and O'Neil, 1991), or elsewhere in cartridges, where other cell types synapse. Second, pairs of such immunoreactive puncta ∽500 nm apart are found around the circumference of the photoreceptor terminal cross section, although the numbers of these apparently exceed the few such pairs of tetrads previously reported with a separation of ≤600 nm (Meinertzhagen and Hu, 1996). Third, the numbers of immunostained puncta,

between 30 and 50 per ∽5 μm length of cartridge (Hiesinger, unpublished observations) in the 3D datasets, are of the same order of magnitude as the numbers of lamina synapses, tetrads or others, found from serial EM but are insufficient to account for all (Meinertzhagen and Sorra, 2000).

The possibility of resolving subcellular details such as synaptic sites underscores the significance of 3D deconvolution approaches in providing new insights into the functional context of identified markers. It also illustrates the major limitation, that the evidence presented is a high-order description indicating only a possible ultrastructural localization or function for the particular protein. In the particular case of n-Syb, further support for the possibility that this localizes at the photoreceptor tetrads will require immuno-EM methods and careful numerical comparisons. On the other hand, the deconvolution analysis provides a much needed method to screen likely markers prior to undertaking more laborious immuno-EM. We are not unaware of the prospect that, once the ultrastructural location of immunostained structures is confirmed by immuno-EM, deconvolved 3D datasets can then be used for efficient quantitative analyses of organelles or other structures of interest, which currently require serial- or quantitative EM reconstructions.

In summary, we have demonstrated both the applicability of the deconvolution method for superior high-resolution images of photoreceptor terminals and the usability of high-resolution data of lamina cross sections to analyze the differential localization of vesicle trafficking molecules within such terminals. Future investigations of molecules underlying the vesicle trafficking and neurotransmitter release machinery thus now have access to a new deconvolution method to contribute fine-structural and localization data to molecular and histological analyses, one that offers considerable advantages over EM as a method to screen such expression in photoreceptor terminals.

LITERATURE CITED

Brand AH, Dormand E-L. 1995. The Gal4 system as a tool for unravelling the mysteries of the *Drosophila* nervous system. Curr Opin Neurobiol 5:572–578.

Burgess RW, Deitcher DL, Schwarz TL. 1997. The synaptic protein syntaxin 1 is required for cellularization of *Drosophila* embryos. J Cell Biol 138:861–875.

Deitcher DL, Ueda A, Stewart BA, Burgess RW, Kidokoro Y, Schwarz TL. 1998. Distinct requirements for evoked and spontaneous release of neurotransmitter are revealed by mutations in the *Drosophila* gene *neuronal-synaptobrevin*. J Neurosci 18:2028–2039.

Denk W, Piston DW, Webb WW. 1995. Two-photon molecular excitation in laser-scanning microscopy. In: Pawley JB, editor. Handbook of biological confocal microscopy. New York: Plenum Press. p 445–458.

Eberle KK, Zinsmaier KE, Buchner S, Gruhn M, Jenni M, Arnold C, Leibold C, Reisch D, Walter N, Hafen E, Hofbauer A, Pflugfelder GO, Buchner E. 1998. Wide distribution of the cysteine string proteins in *Drosophila* tissues revealed by targeted mutagenesis. Cell Tissue Res 294:203–217.

Estes PS, Ho GLY, Narayanan R, Ramaswami M. 2000. Synaptic localization and restricted diffusion of a *Drosophila* neuronal synaptobrevin-green fluorescent protein chimera in vivo. J Neurogenet 13:233–255.

Fischbach KF, Dittrich APM. 1989. The optic lobe of *Drosophila melanogaster*. Part I: a Golgi analysis of wild-type structure. Cell Tissue Res 258:441–475.

Freeman M. 1996. Reiterative use of the EGF receptor triggers differentiation of all cell types in the *Drosophila* eye. Cell 87:651–660.

Fujita SC, Zipursky SL, Benzer S, Ferrús A, Shotwell SL. 1982. Monoclonal antibodies against the *Drosophila* nervous system. Proc Natl Acad Sci USA 79:7929–7933.

Gibson SF, Lanni F. 1992. Experimental test of an analytical model of aberration in an oil-immersion objective lens used in three-dimensional light microscopy. J Opt Soc Am A9:154–166.

Good IJ, Gaskins RA. 1971. Nonparametric roughness penalties for probability densities. Biometrica 58:255–277.

Hiesinger PR, Reiter C, Schau H, Fischbach K-F. 1999. Neuropil pattern formation and regulation of cell adhesion molecules in *Drosophila* optic lobe development depend on synaptobrevin. J Neurosci 19:7548–7556.

Hofbauer A, Campos-Ortega JA. 1990. Proliferation pattern and early differentiation of the optic lobes in *Drosophila melanogaster*. Roux Arch Dev Biol 198:264–274.

Holmes TJ. 1988. Maximum-likelihood image restoration adapted for noncoherent optical imaging. J Opt Soc Am A5:666–673.

Holmes TJ. 1992. Blind deconvolution of quantum-limited incoherent imagery: maximum likelihood approach. J Opt Soc Am A9:1052–1061.

Holmes TJ, Bhattacharyya S, Cooper JA, Hanzel D, Krishnamurthi V, Lin W, Roysam B, Szarowski DH, Turner JN. 1995. Light microscopic images reconstructed by maximum likelihood deconvolution. In: Pawley JB, editor. Handbook of biological confocal microscopy. New York: Plenum Press. p 389–402.

Ito K, Suzuki K, Estes P, Ramaswami M, Yamamoto D, Strausfeld NJ. 1998. The organization of extrinsic neurons and their implications in the functional roles of the mushroom bodies in *Drosophila melanogaster* Meigen. Learn Mem 5:52–77.

Joshi S, Miller MI. 1993. Maximum a posteriori estimation with Good's roughness for three-dimensional optical-sectioning microscopy. J Opt Soc Am A10:1078–1085.

Krantz DE, Zipursky SL. 1990. *Drosophila* chaoptin, a member of the leucine-rich repeat family, is a photoreceptor cell-specific adhesion molecule. EMBO J 9:1969–1977.

Lane RG, Bates RHT. 1987. Automatic multidimensional deconvolution. J Opt Soc Am A4:180–188.

Meinertzhagen IA, Hanson TE. 1993. The development of the optic lobe. In: Bate M, Martinez Arias A, editors. The development of *Drosophila melanogaster*, vol. II. Plainview, NY: Cold Spring Harbor Press. p 1363–1491.

Meinertzhagen IA, Hu X. 1996. Evidence for site selection during synaptogenesis: the surface distribution of synaptic sites in photoreceptor terminals of the flies *Musca* and *Drosophila*. Cell Mol Neurobiol 16: 677–698.

Meinertzhagen IA, O'Neil SD. 1991. Synaptic organization of columnar elements in the lamina of the wild type in *Drosophila melanogaster*. J Comp Neurol 305:232–263.

Meinertzhagen IA, Sorra KE. 2000. Synaptic organisation in the fly's optic lamina: few cells, many synapses and divergent microcircuits. Progr Brain Res (in press).

Pennetta G, Wu MN, Bellen HJ. 1999. Dissecting the molecular mechanism of neurotransmitter release in *Drosophila*. In: Bellen H, editor. Neurotransmitter release. Oxford: Oxford University Press. p 304–351.

Richardson WH. 1972. Bayesian-based iterative method of image restoration. J Opt Soc Am 62:55–59.

Schneider T, Reiter C, Eule E, Bader B, Lichte B, Nie Z, Schimansky T, Ramos GP, Fischbach K-F. 1995. Restricted expression of the IrreC-rst protein is required for normal axonal projections of columnar visual neurons. Neuron 15:259–271.

Scholz M, Stetter M, Obermayer K. 1998. Deblurring of confocal microscope images: tissue properties, optics and simulations. Soc Neurosci Abstr 24:1060.

Scholz M, Bucher D, Pflüger H-J, Obermayer K. 1999. Correction schemes for geometrically exact 3D reconstructions of neurons from confocal images. Soc Neurosci Abstr 25:1508.

Schulze KL, Bellen HJ. 1996. *Drosophila* syntaxin is required for cell viability and may function in membrane formation and stabilization. Genetics 144:1713–1724.

Stark WS, Carlson SD. 1986. Ultrastructure of capitate projections in the optic neuropil of Diptera. Cell Tissue Res 246:481–486.

Stowers SR, Schwarz T. 1999. A genetic method for generating *Drosophila* eyes composed exclusively of mitotic clones of a single genotype. Genetics 152:1631–1639.

Strausfeld NJ, Meinertzhagen IA. 1998. The insect neuron: types, morphologies, fine structure, and relationship to the architectonics of the insect nervous system. In: Harrison FW, Locke M, editors. Microscopic anatomy of invertebrates, vol. 11B: Insecta. New York: Wiley-Liss. p 487–538.

Timmons L, Becker J, Barthmaier P, Fyrberg C, Shearn A, Fyrberg E. 1997. Green fluorescent protein/beta-galactosidase double reporters for visualizing *Drosophila* gene expression patterns. Dev Genet 20:338–347.

Van Vactor D Jr, Krantz DE, Reinke R, Zipursky SL. 1988. Analysis of mutants in chaoptin, a photoreceptor cell-specific glycoprotein in *Drosophila*, reveals its role in cellular morphogenesis. Cell 52:281–290.

Verveer PJ, Jovin TM. 1998. Image restoration based on Good's roughness penalty with application to fluorescence microscopy. J Opt Soc Am A15:1077–1083.

Weber T, Zemelman BV, McNew JA, Westermann B, Gmachl M, Parlati F, Sollner TH, Rothman JE. 1998. SNAREpins: minimal machinery for membrane fusion. Cell 92:759–772.

Zinsmaier KE, Hofbauer A, Heimbeck G, Pflugfelder GO, Buchner S, Buchner E. 1990. A cysteine-string protein is expressed in retina and brain of *Drosophila*. J Neurogenet 7:15–29.

Zinsmaier KE, Eberle KK, Buchner E, Walter N, Benzer S. 1994. Paralysis and early death in cysteine string protein mutants of *Drosophila*. Science 263:977–980.

Zipursky SL, Venkatesh TR, Teplow DB, Benzer S. 1984. Neuronal development in the *Drosophila* retina: monoclonal antibodies as molecular probes. Cell 36:15–26.